

Marquette University

e-Publications@Marquette

Mathematics, Statistics and Computer Science Faculty Research and Publications Mathematics, Statistics and Computer Science, Department of (- 2019)

1-2014


A Statistical fMRI Model for Differential T_2^* Contrast Incorporating T_1 and T_2^* of Gray Matter

M. Muge Karaman
Marquette University

Iain P. Bruce
Marquette University

Daniel B. Rowe
Marquette University, daniel.rowe@marquette.edu

Follow this and additional works at: https://epublications.marquette.edu/mscs_fac

 Part of the [Computer Sciences Commons](#), [Mathematics Commons](#), and the [Statistics and Probability Commons](#)

Recommended Citation

Karaman, M. Muge; Bruce, Iain P.; and Rowe, Daniel B., "A Statistical fMRI Model for Differential T_2^* Contrast Incorporating T_1 and T_2^* of Gray Matter" (2014). *Mathematics, Statistics and Computer Science Faculty Research and Publications*. 204.
https://epublications.marquette.edu/mscs_fac/204

Marquette University

e-Publications@Marquette

Mathematics and Statistical Sciences Faculty Research and Publications/College of Arts and Sciences

This paper is NOT THE PUBLISHED VERSION; but the author's final, peer-reviewed manuscript. The published version may be accessed by following the link in the citation below.

Magnetic Resonance Imaging, Vol. 32, No. 1 (January 2014): 9-27. [DOI](#). This article is © Elsevier and permission has been granted for this version to appear in [e-Publications@Marquette](#). Elsevier does not grant permission for this article to be further copied/distributed or hosted elsewhere without the express permission from Elsevier.

A Statistical fMRI Model for Differential T_2^* Contrast Incorporating T_1 and T_2^* of Gray Matter

M. Muge Karaman

Department of Mathematics, Statistics, and Computer Science, Marquette University, Milwaukee, WI

Iain P. Bruce

Department of Mathematics, Statistics, and Computer Science, Marquette University, Milwaukee, WI

Daniel B. Rowe

Department of Mathematics, Statistics, and Computer Science, Marquette University, Milwaukee, WI

Department of Biophysics, Medical College of Wisconsin, Milwaukee, WI

Abstract

Relaxation parameter estimation and brain activation detection are two main areas of study in magnetic resonance imaging (MRI) and functional magnetic resonance imaging (fMRI). Relaxation parameters can be used to distinguish voxels containing different types of tissue whereas activation determines voxels that are associated with neuronal activity. In fMRI, the standard practice has been to discard the first scans to avoid

magnetic saturation effects. However, these first images have important information on the MR relaxivities for the type of tissue contained in voxels, which could provide pathological tissue discrimination. It is also well-known that the voxels located in gray matter (GM) contain neurons that are to be active while the subject is performing a task. As such, GM MR relaxivities can be incorporated into a statistical model in order to better detect brain activation. Moreover, although the MR magnetization physically depends on tissue and imaging parameters in a nonlinear fashion, a linear model is what is conventionally used in fMRI activation studies. In this study, we develop a statistical fMRI model for Differential T_2^* ConTrast Incorporating T_1 and T_2^* of GM, so-called DeTeCT-ING Model, that considers the physical magnetization equation to model MR magnetization; uses complex-valued time courses to estimate T_1 and T_2^* for each voxel; then incorporates gray matter MR relaxivities into the statistical model in order to better detect brain activation, all from a single pulse sequence by utilizing the first scans.

Keywords

MRI, fMRI, Complex-valued fMRI analysis, Differential T_2^* contrast, Relaxation parameter estimation

1. Introduction

The spin density, longitudinal relaxation time, T_1 , and transverse relaxation time, T_2^* , provide the three most intrinsic and basic contrast mechanisms in MRI/fMRI. It is thus of interest to measure and exploit differences in these parameters in order to develop image contrast between different brain tissue since the resulting measured values could be used for tissue characterization and provide useful information on local environment interaction. The quantization of the relaxation parameters helps to predict both the signal-to-noise ratio (SNR) and the contrast-to-noise ratio (CNR) for a given sequence and makes it possible to better understand the contrast mechanism and the tissue characterization.

The Bloch equations describe the behavior of a magnetization vector in the presence of an externally applied magnetic field subject to the relaxation process [1]. According to the solution of the Bloch equations, magnetization can be characterized by the tissue parameters (T_1 , T_2 or T_2^* , M_0) and imaging parameters (TR, TE, ϕ) where TR is the repetition time, TE is the echo time, and ϕ is the flip angle. Thus, the signal change can be induced by a change in spin density, T_1 , and/or T_2^* . In a T_2^* -weighted gradient echo (GRE) fMRI experiment, for a stationary voxel, the magnetization after the t^{th} excitation, M_t , for a series of excitations is given by:

(1)

$$M_t = \left[M_{t-1} e^{-\frac{TR}{T_1}} \cos(\phi) + M_0 \left(1 - e^{-\frac{TR}{T_1}} \right) \right] \sin(\phi) e^{-\frac{TE_t}{T_2^*}}.$$

Accurate relaxation parameter estimation is essential in quantitative MR applications as being a fundamental way of determining image segmentation and tissue characterization as well as quantifying absolute metabolites in NMR spectroscopy. A quantitative analysis of T_2 can give useful information for cancer discrimination [2]. Moreover, tissue characterization may serve as a very important source of information in detecting brain activation since it is generally believed that gray matter tissue includes the neurons that are to be active during the performance of a task. Considering the fact that fMRI images are based on hemodynamic changes related to neuronal activity, and not the electrical activity itself, the accuracy of the brain activation statistics calculated from the considered statistical fMRI activation model plays a major role for the medical statements that could be drawn. As such, incorporation of the information of the tissue characteristics into the brain activation detection process can provide more accurate activation statistics by theoretically eliminating the false positives.

Using only the magnitude of complex-valued magnetic resonance images has become the gold standard for the estimation of the relaxation parameters although voxel time courses in fMRI are complex-valued [3], [4], [5], [6], [7], [8]. However, Baseline et al. recently presented a statistical technique to estimate relaxation times exploiting complex-valued MR images [9]. Wheaton et al. [10] reconstructed $T_1\rho$ maps from partial k -space image data using linear regression, and error was measured with relation to $T_1\rho$ maps created from the full k -space images. Haldar et al. utilized the variable projection algorithm for maximum likelihood estimation of T_1 relaxation parameters by reducing the four-dimensional minimization problem to a two dimensional maximization problem, rather than iteratively solving the 4-parameter curve fitting problem [4].

In fMRI, voxel time courses are complex-valued after Fourier, or non-Fourier image reconstruction due to the phase imperfections as a result of magnetic field inhomogeneities. Although important functional information can be inferred from the phase [11], [12], [13], [14], [15], it has been a common practice in fMRI to determine functional brain activation from the magnitude-only data model which discards the phase information [16], [17]. A complex-valued fMRI activation model was presented by Rowe and Logan [14] to determine functional brain activation and it was shown that the use of complex-valued data provides an improved power of detection at low SNRs and low CNRs. Therefore, the statistical fMRI model for detecting activation introduced in this study is based upon the complex-valued activation model of Rowe and Logan.

In this manuscript, we develop a statistical fMRI model for Differential T_2^* ConTrast Incorporating T_1 and T_2^* of GM, so-called DeTeCT-ING Model, to determine brain activation by incorporating T_1 and T_2^* of gray matter [18]. The model considers the physical nonlinear signal equation to model MR magnetization rather than using a linear model; utilizes the first scans of the complex-valued fMRI data to estimate each voxel's T_1 and T_2^* ; and incorporates GM T_1 and T_2^* values into the activation statistics. A single pulse sequence is utilized with three parts, where in the first two parts the subject does not perform the task while in the third part the subject performs the task as in a standard fMRI experiment. In the first part, several images are acquired at a constant TE; in the second part, TE is varied; and in the third part TE is constant. This pulse sequence allows one to have the three parts for: a) T_1 estimation, b) T_2^* estimation and c) detecting activation, while all of the model parameters are estimated simultaneously using data from the entire scan. The parameter setting in the first part allows the utilization of signal change between data acquired during the transient state prior to T_1 equilibrium and the steady state images since the volumes at the beginning of fMRI block contains a transition signal and the signal of the first EPI volume is $M_1 = M_0 e^{-TE/T_1}$. The second and third parts of the pulse sequence differentiate the signal with TE and differential task changes respectively since T_2^* is influenced by TE, and activation is modeled by differential signal change. Furthermore, a slightly modified version of the DeTeCT-ING Model, so-called DeTeCT Model, is developed by modeling the complex-valued observations according to the physical magnetization equation, utilizing the first scans to estimate the MR relaxivities, but not incorporating GM T_2^* and T_1 values into the activation statistics in order to observe the benefits of GM MR relaxivities incorporation on the computed activation statistics. The Cramer–Rao Lower Bounds (CRLBs), which provide a lower bound for the variance of unbiased parameter estimators, are also numerically calculated for DeTeCT-ING and DeTeCT Models.

In order to observe the performance of the DeTeCT-ING model, theoretical illustrations are implemented on 96×96 phantom data through simulation and the model is compared with the conventionally used magnitude-only (MO) and newer complex-valued (CV) fMRI activation models by comparing the means and variances of the model parameters and activation statistics with the true parameter values and CRLBs of the models. The DeTeCT-ING model is then evaluated by deploying all four models, DeTeCT-ING, DeTeCT, MO, and CV, in the acquired bilateral finger tapping fMRI data.

2. Theory

2.1. Complex-valued (CV) fMRI Activation Model

After the inverse Fourier transform, images or voxel measurements are complex-valued and still corrupted by noise in both real and imaginary parts [14].

The complex-valued image measured over time in a given voxel is:

(2)

$$y_{CV_t} = (M_{CV_t} \cos\theta + \eta_{R_t}) + i(M_{CV_t} \sin\theta + \eta_{I_t}),$$

$$t = 1, \dots, n$$

where $(\eta_{R_t}, \eta_{I_t})' \sim N(0, \Sigma)$, the true population magnitude is M_{CV_t} , and θ is phase. It is generally assumed that $\Sigma = \sigma^2 I_2$.

The data gathered during the course of an fMRI experiment are comprised of a sequence of individual MR images acquired while the subject performs a set of tasks. Throughout the experiment, the subject generally alternates between performing no task and performing a task allowing the task-related activations to be detected by qualifying the relative changes in the measured signal between individual images. The task-related activations are detected by qualifying the relative changes in the measured signal between individual images. Using periods of non-task scans is a common means of establishing a baseline on which the assumption is made that the brain activity scales in a linear fashion. A linear model is generally used to describe the temporally varying magnitude M_{CV_t} :

(3)

$$M_{CV_t} = x'_t \beta = \beta_t + \beta_1 x_{1t} + \dots + \beta_q x_{qt},$$

where q is the number of non-baseline regressors, x_t is the t^{th} row of an $n \times (q + 1)$ design matrix X , β is a $(q + 1) \times 1$ vector of magnitude regression coefficients, and the operator $'$ denotes the transpose of a vector. Thus, the observed complex-valued data at time t can be represented by a 2×1 real-valued vector,

(4)

$$\begin{pmatrix} y_{R_t} \\ y_{I_t} \end{pmatrix} = \begin{pmatrix} x'_t \beta \cos\theta \\ x'_t \beta \sin\theta \end{pmatrix} + \begin{pmatrix} \eta_{R_t} \\ \eta_{I_t} \end{pmatrix},$$

where y_{R_t} is the real part and y_{I_t} is the imaginary part of the observed image-space data at time point, t .

This model can also be written more generally as

(5)

$$y_{CV} = \begin{pmatrix} X & 0 \\ 0 & X \end{pmatrix} \begin{pmatrix} \beta \cos\theta \\ \beta \sin\theta \end{pmatrix} + \eta$$

$$2n \times 1 \quad 2n \times 2(q + 1) \quad 2(q + 1) \times 1 \quad 2n \times 1$$

where the observed vector of data $y_{CV} = (y'_{R_t}, y'_{I_t})'$ is the vector of observed real values stacked on the observed imaginary values and the vector of errors $\eta = (\eta'_{R_t}, \eta'_{I_t})' \sim N(0, \Sigma \otimes \Phi)$ is similarly defined. It is generally assumed that $\Sigma = \sigma^2 I_2$ and $\Phi = I_n$.

FMRI does not directly measure the electrical activity of the neurons, but the change in blood oxygenation indirectly caused by that activity. Thus, model parameters are estimated under the appropriately constrained null and alternative hypotheses, $H_0: C\beta = 0$ versus $H_1: C\beta \neq 0$, after which activation is determined with a generalized likelihood ratio statistic.

Unrestricted MLE's of the parameters, phase, $\hat{\theta}$, regression coefficients, $\hat{\beta}$, and variance, $\hat{\sigma}^2$, under the alternative hypothesis, $H_1: C\beta \neq 0$, can be derived by maximizing the logarithm of the likelihood function and yields

(6)

$$\hat{\theta} = \frac{1}{2} \tan^{-1} \left[\frac{2\hat{\beta}'_R (X'X)\hat{\beta}_I}{\hat{\beta}'_R (X'X)\hat{\beta}_R - \hat{\beta}'_I (X'X)\hat{\beta}_I} \right]$$

$$\hat{\beta} = \hat{\beta}_R \cos \hat{\theta} + \hat{\beta}_I \sin \hat{\theta}$$

$$\hat{\sigma}^2 = \frac{1}{2n} \left[y - \begin{pmatrix} X\hat{\beta} \cos \hat{\theta} \\ X\hat{\beta} \sin \hat{\theta} \end{pmatrix} \right]' \left[y - \begin{pmatrix} X\hat{\beta} \cos \hat{\theta} \\ X\hat{\beta} \sin \hat{\theta} \end{pmatrix} \right]$$

where the estimate of the regression coefficients from the real part of the time series under the alternative hypothesis is $\hat{\beta}_R = (X'X)^{-1}X'y_R$ and the estimate of the regression coefficients from the imaginary part of the time series under the alternative hypothesis is $\hat{\beta}_I = (X'X)^{-1}X'y_I$ [14], [15], [20].

The MLE's of the parameters, phase, $\tilde{\theta}$, regression coefficients, $\tilde{\beta}$, and variance, $\tilde{\sigma}^2$, under the constrained null hypothesis, $H_0: C\beta = 0$, can also be derived by maximizing the logarithm of the likelihood function with the Lagrange multiplier term $\Psi'(C\beta - 0)$ and yields

(7)

$$\tilde{\theta} = \frac{1}{2} \tan^{-1} \left[\frac{2\hat{\beta}'_R \Psi(X'X)\hat{\beta}_I}{\hat{\beta}'_R \Psi(X'X)\hat{\beta}_R - \hat{\beta}'_I \Psi(X'X)\hat{\beta}_I} \right]$$

$$\tilde{\beta} = \Psi[\hat{\beta}_R \cos \tilde{\theta} + \hat{\beta}_I \sin \tilde{\theta}]$$

$$\tilde{\sigma}^2 = \frac{1}{2n} \left[y - \begin{pmatrix} X\tilde{\beta} \cos \tilde{\theta} \\ X\tilde{\beta} \sin \tilde{\theta} \end{pmatrix} \right]' \left[y - \begin{pmatrix} X\tilde{\beta} \cos \tilde{\theta} \\ X\tilde{\beta} \sin \tilde{\theta} \end{pmatrix} \right]$$

where Ψ is

(8)

$$\Psi = I_{q+1} - (X'X)^{-1}C'[C(X'X)^{-1}C']^{-1}C$$

[14], [15], [20].

Denoting the maximum likelihood estimators under the alternative hypothesis using hats, and those under the null hypothesis using tildes, the generalized likelihood ratio statistics for the CV model, $-2\log\lambda_C$, can be derived as,

(9)

$$-2\log\lambda_C = 2n\log\left(\frac{\tilde{\sigma}^2}{\hat{\sigma}^2}\right),$$

where λ_C is the likelihood ratio statistics and n is the number of time points in the fMRI experiment.

This statistic has an asymptotic χ_r^2 distribution in large samples, where r is the difference in the number of constraints between the alternative and the null hypotheses or the full row rank of C . Note that, when $r = 1$, two-sided testing can be performed using the signed likelihood ratio test given by

(10)

$$Z_C = \text{sign}(C\hat{\beta})\sqrt{-2\log\lambda_C}$$

which in large samples has an approximate standard normal distribution under the null hypothesis [14], [19].

With the given distributional specifications, the CRLBs can be computed from the likelihood of the complex-valued data [20].

2.2. Magnitude-Only (MO) fMRI Activation Model

In fMRI, complex-valued time courses are almost exclusively converted to magnitude and phase time courses, then the magnitude-only activation is detected while phase voxel time courses are discarded [16], [17]. This typical method to compute the activation using only the magnitude at time t , denoted by y_{MOt} is written as

(11)

$$y_{MOt} = \left[\left(M_{MOt} \cos\theta + \eta_{Rt} \right)^2 + \left(M_{MOt} \sin\theta + \eta_{It} \right)^2 \right]^{\frac{1}{2}},$$

where $(\eta_{Rt}, \eta_{It})' \sim N(0, \sigma^2 I_2)$ and true population magnitude, M_{MOt} , is given by Eq. (3).

The magnitude of a complex-valued observation at time t is not normally distributed but is Ricean distributed [21], [22], [14]. The Ricean distribution of the magnitude y_{MOt} at time t becomes normal with mean $x'\beta$ and variance σ^2 at high SNRs.

This model can also be written as

(12)

$$\begin{matrix} y_{MO} & & = & X & & \beta & + & \varepsilon \\ n \times 1 & & & n \times 1(q+1) & & (q+1) \times 1 & & n \times 1' \end{matrix}$$

where $\varepsilon \sim N(0, \sigma^2 \Phi)$, Φ is the temporal correlation matrix often taken to be $\Phi = I_n$ after pre-whitening of the data.

Assuming a normal distribution for the errors in Eq. (12), the unconstrained maximum likelihood estimates of the parameters (β, σ^2) can be derived as

(13)

$$\hat{\beta} = (X'X)^{-1}X'm$$

$$\hat{\sigma}^2 = (m - X\hat{\beta})'(m - X\hat{\beta})/n.$$

In order to construct a generalized likelihood ratio test of the hypothesis $H_0: C\beta = 0$ versus $H_1: C\beta \neq 0$, where C is a full row rank matrix, the likelihood under the constrained hypothesis is maximized. The constrained MLE's can be derived as

(14)

$$\tilde{\beta} = \Psi\hat{\beta}$$

$$\tilde{\sigma}^2 = (m - X\tilde{\beta})'(m - X\tilde{\beta})/n,$$

where Ψ is defined as in Eq. (8).

Similarly with the complex activation model, the likelihood ratio statistics for the MO are given by,

(15)

$$-2\log\lambda_M = n\log\left(\frac{\tilde{\sigma}^2}{\hat{\sigma}^2}\right).$$

The likelihood ratio test has an asymptotic χ_1^2 distribution and is asymptotically equivalent to the usual t tests for activation given by

(16)

$$t = \frac{\hat{\beta}_2}{SE(\hat{\beta}_2)}.$$

With the given distributional specifications, the CRLBs can be computed from the likelihood of the magnitude-only data [20].

2.3. DeTeCT-ING and DeTeCT fMRI Activation Models

2.3.1. Modeling fMRI Data

The temporally varying magnitude of the signal can be represented by incorporating the effect of the task execution to the magnetization. In the DeTeCT-ING and DeTeCT Models, the temporally varying magnitude, M_t , for an individual voxel, is defined as

(17)

$$M_t = \left[M_t e^{-\frac{TR}{T_1}} \cos(\phi) + M_0 \left(1 - e^{-\frac{TR}{T_1}} \right) \right] \sin(\phi) e^{-\frac{TE_t}{T_2^* + \delta z_t}} + x_t \beta_1.$$

where $x_t' \beta_1 = \beta_1 x_t$.

In this model, δ is the differential signal change, which is a coefficient for a reference function z_t related to a block experimental design. As noted before, brain activation causes changes in blood oxygenation leading to

changes in decay parameter, T_2^* . Therefore, the parameter δz_t is included with the decay parameter T_2^* in the exponential function. The coefficient β_1 is the coefficient for a time trend t for all voxels.

The complex-valued observations at time t can then be described as

(18)

$$y_t = \left[\left(M_{t-1} e^{-TR/T_1} \cos(\phi) + M_0 (1 - e^{-TR/T_1}) \right) \sin(\phi) e^{-TE_t/T_2^* + \delta z_t} + x_t \beta_1 \right] (\cos \theta_t + i \sin \theta_t) + (\eta_{R_t} + i \eta_{I_t})$$

where $(\eta_{R_t}, \eta_{I_t})' \sim N(0, \Sigma)$ and it can be assumed that $\Sigma = \sigma^2 I_2$ as in Eq. (5).

2.3.2. Estimation of the Model Parameters

Least Squares (LS) estimation is a method of estimating parameters by minimizing the squared discrepancies on the observed data and their expected values. Working in the complex domain with the data having normally distributed noise and dealing with an over determined system allows for the use of a LS estimator, which is a computationally convenient measure of fit. As the unknown parameters of this model, $(M_0, T_1, T_2^*, \delta, \beta_1, \vartheta)$ are nonlinear in the representation of the magnetization given by Eq. (18), a nonlinear LS estimation can be implemented.

The nonlinear LS estimator, $\hat{\Gamma}(M_0, T_1, T_2^*, \delta, \beta_1, \vartheta)$ is obtained by minimizing the function,

(19)

$$\begin{aligned} \sigma^2 (M_0, T_1, T_2^*, \delta, \beta_1, \vartheta | y_{R_t}, y_{I_t}, TR, \phi, TE_t, z_t) \\ = \frac{1}{2n} \sum_{t=1}^n \left[(y_{R_t} - M_t \cos \theta)^2 + (y_{I_t} - M_t \sin \theta)^2 \right], \end{aligned}$$

with respect to the unknown parameters, $M_0, T_1, T_2^*, \delta, \beta_1, \vartheta$; where M_t is given by Eq. (17). In this objective function, $y_t = y_{R_t} + i y_{I_t}$ is the observed signal of an individual voxel at time t ; and $M_t \cos \theta$ and $M_t \sin \theta$ are the expected real and imaginary parts of the signal.

It is well known that the LS procedure corresponds to the maximum likelihood estimate (MLE) when appropriate probabilistic assumptions about underlying error distributions can be made, as in the proposed model. Since the nonlinear LS problem has no closed solution and is usually solved by iterative refinement, the parameters of the model will be determined numerically.

2.3.3. fMRI Activation

The main issue in analyzing functional MRI images is comparing images in a statistically meaningful way. In this study, the simple matter of detecting 'activation', the local increase in the effect of the task, with most of the brain unaffected by the task, is the primary focus of study. The model parameters are estimated under appropriately constrained null and alternative hypotheses, after which activation is determined, which is characterized by differential T_2^* contrast, δ , with a generalized likelihood ratio statistic.

According to the parameterization in the setting of the DeTeCT-ING Model, "active" or "on" regions in the brain contain voxels with values $T_1 = T_{1GM}$, $T_2^* = T_{2^*GM}$ and $\delta \neq 0$ while "inactive" or "off" regions contain voxels with $T_1 = T_{1GM}$, $T_2^* = T_{2^*GM}$ and $\delta = 0$ where T_{1GM} and T_{2^*GM} are GM T_1 and T_2^* values.

Maximum likelihood estimates of the parameters ($M_0, T_1, T_2^*, \delta, \beta_1, \vartheta$) can then be determined for both restricted alternative and null hypotheses. The hypotheses pair,

(20)

$$H_0: T_1 = T_{1_{GM}}, T_2^* = T_{2^*_{GM}}, \delta = 0 \text{ vs } H_1: T_1 = T_{1_{GM}}, T_2^* = T_{2^*_{GM}}, \delta \neq 0$$

detects task related voxel activation in GM.

According to the parameterization in the setting of the DeTeCT Model, “active” or “on” regions in the brain contain voxels with values $\delta \neq 0$ while “inactive” or “off” regions contain voxels with $\delta = 0$. Maximum likelihood estimates of the parameters ($M_0, T_1, T_2^*, \delta, \beta_1, \vartheta$) can be determined for both restricted alternative and null hypotheses. The hypotheses pair, (21) $H_0: \delta = 0$ vs. $H_1: \delta \neq 0$ detects task related voxel activation without consideration of the tissue type.

Parameter estimates under the null hypothesis, ($\tilde{M}_0, \tilde{T}_1, \tilde{T}_2^*, \tilde{\delta}, \tilde{\beta}_1, \tilde{\vartheta}$), and the alternative hypothesis, ($\hat{M}_0, \hat{T}_1, \hat{T}_2^*, \hat{\delta}, \hat{\beta}_1, \hat{\vartheta}$), for the models can be determined by numerical minimization of Eq. (19) with respect to the parameters. The generalized likelihood ratio statistics, λ_c , the ratio of restricted null over alternative hypotheses lead to the large sample χ_1^2 distributed statistic, $-2\log\lambda_c$ that is given in Eq. (9). Two-sided testing can then be performed using the signed likelihood ratio test given by Eq. (10).

3. Methods and materials

3.1. Simulated data

3.1.1. Part I: Simulated Phantom Data with the Fixed Parameter Setting

The first part of the simulation study theoretically illustrates the properties of the parameter estimates for the introduced models. For this part, a 96×96 slice of the human head with two 7×7 region of interests (ROIs) was realistically simulated according to the Shepp–Logan phantom standards [23]. Data for all models were generated to simulate voxel activation from a bilateral finger tapping fMRI block design experiment. The block design consisted of 20 s off followed by sixteen epochs of 15 s on and 15 s off with TR = 1 s. The simulation consisted of $n = 510$ time points where the true activation structure is known to be within ROIs so that the model can be evaluated. The considered ROIs that are designated to have activation are shown in Fig. 1. The presented results for this part of our simulation study are calculated over 500 simulations.

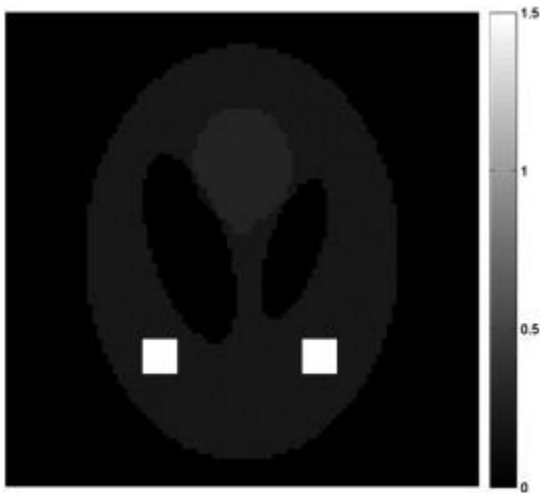


Fig. 1. Anatomical mask with ROIs.

The spin density and the relaxation parameter values of the simulated tissues measured at 3.0-T are given in Table 1 [24]. The parameter values of the voxels that consist of different kinds of tissue were obtained by averaging their values. For all voxels inside the phantom in this simulation, the phase and the flip angles were generically selected to be $\vartheta = 45^\circ$, $\phi = 90^\circ$ while $\beta_1 = .01$ and $\sigma = .01$. The differential T_2^* contrast, δ , was given a constant value of 1 for the voxels in ROIs while defined to be zero for the inactive regions. The true maps of the true spin density, M_0 ; longitudinal relaxation, T_1 ; transverse relaxation, T_2^* ; differential T_2^* contrast, δ ; linear trend, β_1 , and phase angle, ϑ are illustrated in Figs. 2a, b, c, d, e and f, respectively.

Table 1. Spin density and the relaxation times in milliseconds for the Shepp–Logan Phantom.

Tissue	M_0	T_1	T_2^*
CSF	1	4000	2200
Gray Matter (GM)	0.83	1331	42
White Matter (WM)	0.71	832	49

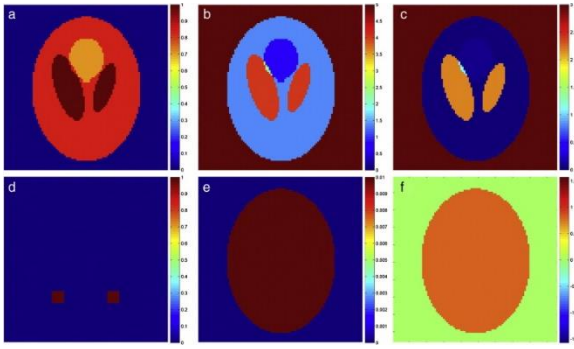


Fig. 2. True parameter maps for DeTeCT and DeTeCT-ING Models generated according to 2D Shepp–Logan phantom standards for a 96×96 slice. a) True M_0 map, b) true T_1 map in s., c) true T_2^* map in s., d) true δ map, e) true β_1 map, f) true ϑ map.

Simulated fMRI data are generated according to the proposed model given by Eqs. (17), (18). An fMRI block design experiment with an acquisition of 510 repetitions was used to estimate the model parameters. For each voxel, time depending echo time, TE_t , was assumed to consist of three parts. In the first part, it is fixed as having a value of 42.7 ms at the first 10 time points. In the second part, the first 5 TE values are equispaced in the interval [42.7 ms, 52.7 ms] that consists of the following TE values: 42.7, 45.2, 47.7, 50.2, 52.7, and this procedure is repeated again for the next 5 time points. Finally, the last 490 TE values are fixed as 42.7 ms as illustrated in Fig. 3a. The time trend X is a column of counting numbers, where the reference function, z_t , which is illustrated in Fig. 3b, consists of blocks of 0's and 1's, as being related to the block experimental design. It can be noted here that a better simulation may be performed with an assumption of very short T_2^* ($<10^{-6}$ ms.) values outside the phantom image.

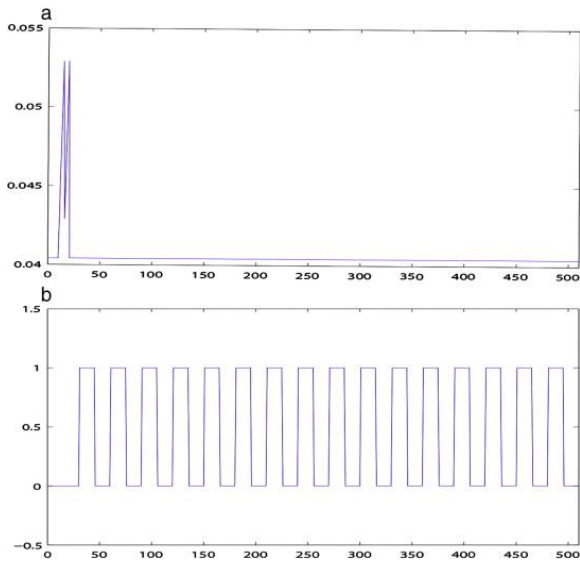


Fig. 3. Imaging parameters. a) Echo time, TE_t ; b) reference function, z_t .

3.1.2. Part II: Simulated Data of Two Voxels with the Varying Parameter Setting

In this simulation study, we evaluate the performances of the considered models for detecting activation with the use of the data generated from one active GM voxel as in an ROI area and one inactive GM voxel from outside of the ROIs at varying parameter settings. For an effective evaluation of the models' performances, we created two sets of scenarios in which we vary a specific parameter and analyze the models' detection performances under these settings. These scenarios were created with the following parameter settings: a) to analyze the models at different levels of the effect of the neural activity in the signal: differential T_2^* contrast, δ , values of the active voxel varying from 0 to 1 with increments of 0.01, $\sigma = 0.5$, and threshold significance level, $\alpha = 0.05$; b) to analyze the sensitivity of the models to the pre-specified α level: threshold significance level, α , varying from 0.01 to 0.1 with steps of 0.0009, $\sigma = 0.5$, and $\delta = 0.1$ for the active voxel. The values of the fixed σ and δ were selected as 0.5 and 0.1, respectively to better observe the efficacy of the models in the presence of high standard deviation noise level and low neural activity effect in the signal. All the other imaging parameters were selected as the same as the ones in Part I. The number of simulations that were performed for both voxels in each scenario was 1000. This simulation was used to measure the accuracy of each model in recognizing the presence of the activation and inactivation in order to compare the accuracy of the models' outcomes with the known activation schemes.

Furthermore, in order to better analyze the overall performances of the models by presenting the connection between the CRLBs and computed sample variances, we created Scenario "c" in which the data of the single active voxel were generated similarly to Scenario "a", with δ values varying from 0 to 1 with increments of 0.1 and threshold significance level, $\alpha = 0.05$. For this scenario, we selected σ to be 0.01 in order to get the same signal properties in our phantom simulation in Part I. The number of simulations that were performed in Scenario "c" was 1000.

3.2. Human Subject Data

To observe the performance of the proposed model in experimental data, an fMRI experiment was performed on a single subject on a 3.0-T General Electric Signa LX magnetic resonance imager. A bilateral finger-tapping task was performed with a visual cue indicating whether to tap or rest. The paradigm followed a block design with an initial 20 s rest followed by 16 epochs of 15 s on and 15 s off. The data sets were composed of seven 2.5-mm-thick axial slices that are 96×96 in dimension for a 24-cm FOV, with the phase encoding direction oriented as posterior to anterior (top-bottom in images). A single slice was selected for analysis. Acquired for a series of

510 TRs, the data sets had a TR of 1 s, a flip angle of 90° and an acquisition bandwidth of 125 kHz. A time varying TE array as it was explained in the theoretical methods was utilized.

As a common practice in fMRI studies, the first 3–5 observations are normally discarded and the reference function is usually designed to be related to a block design consisting of epochs of on and offs starting at the 10th time point with a constant TE. As such, the signal that is acquired for the DeTeCT and DeTeCT-ING Models at the 10th–19th time points is not acquired for MO and CV Models. In order to imitate this common practice, the first 20 observations were excluded before applying CV and MO Models to both simulated and acquired human brain data. Unlike traditional studies, these first observations were not discarded in the DeTeCT and DeTeCT-ING Models as they contain information on different tissue characterization. Parameter estimates of the DeTeCT and DeTeCT-ING Models were determined by numerical minimization of Eq. (19) with the use of MATLAB's optimization toolbox. Activation from $-2\log\lambda$ likelihood ratio statistics which are given in Eq. (15) for MO Model and Eq. (9) for CV, DeTeCT and DeTeCT-ING Models, was thresholded at a 5% Bonferroni family-wise error rate [25]. All programs were written in the MATLAB programming language on a dual quad-core PC with 24 gigabytes of RAM running Microsoft Windows 7.

4. Results

4.1. Analysis

To observe the performance of the proposed methods, the true parameter values and the theoretical minimum standard deviations are compared to the sample means and sample standard deviations of the model parameters computed from the simulation study presented in Part I of Section 3.1. The parameter values that are used to generate data for our simulation study are used for the true values of the parameters the DeTeCT and DeTeCT-ING Models have. For the parameter that only CV and MO Models have, the analytically driven MLEs are used to compute true parameter values from the data with no added noise. Furthermore, the analytically driven CRLBs are used to calculate the theoretical minimum standard deviations for CV and MO Models [20], [26], [27] whereas the CRLBs of the DeTeCT and DeTeCT-ING Models are numerically calculated. The derivations of the analytical expressions for the derivatives of the likelihood function of the DeTeCT and DeTeCT-ING Models, which are used to numerically compute THE CRLBs of the model parameters, are given in Appendix A. CLRBS provide a quantitative measure of the attainable precision of the parameter estimates from a given set of observations. They give insight into the potential performance of the estimators, the performance of the implementation and computation of the estimation models, and the efficiency of the estimators.

In order to better compare the estimated results and the theoretical values, the average voxel values of the descriptive statistics for each tissue type (GM: gray matter, WM: white matter, CSF, Out: outside brain, and ROI) for the parameters estimated under the alternative and null hypotheses are presented in Table 2, Table 3, Table 4, Table 5, Table 6, Table 7, Table 8, Table 9. The first columns that correspond to each parameter represent the true value/theoretical minimum standard deviation values, the second and third columns represent the sample mean/standard deviation values computed from the null (Null) and the alternative (Alt) hypothesis, respectively. In the tables, the power of the estimation is given with a formatting code as regular represents the theoretical value, italic represents a "good", bold represents a "fair", and bold italic represents a "poor" estimate.

Table 2. The average voxel values of the CV Model mean maps.

MEAN	β_0			β_1			β_2			ϑ			σ^2		
	β_0 True	β_0 Alt	β_0 Null	β_1 True	β_1 Alt	β_1 Null	β_2 True	β_2 Alt	β_2 Null	ϑ True	ϑ Alt	ϑ Null	σ^2 True	σ^2 Alt	σ^2 Null
GM	2.708	2.708	2.708	0.01	0.0100	0.01	3.80E-16	-4.41E-08	0	0.7854	0.7854	0.7854	0.0001	9.96E-05	0.0001
WM	2.758	2.758	2.758	0.01	0.0100	0.01	1.64E-16	2.95E-07	0	0.7854	0.7854	0.7854	0.0001	9.96E-05	0.0001
CSF	2.757	2.757	2.757	0.01	0.0100	0.01	2.09E-16	-2.06E-06	0	0.7854	0.7854	0.7854	0.0001	9.96E-05	0.0001
Out	1.25E-14	-1.02E-06	-4E-07	1E-17	-2.38E-09	-2.1E-09	6.16E-31	1.24E-06	0	0.0000	0.0002	-0.0005	0.0001	9.95E-05	0.0001
ROI	2.7076	2.7076	2.8322	0.0100	0.0100	0.0100	0.2542	0.2542	0	0.7854	0.7854	0.7854	0.0001	9.96E-05	0.0002

Table 3. The average voxel values of the CV Model standard deviation maps.

SD	β_0			β_1			β_2			ϑ			σ^2		
	β_0 Min. Theo.	β_0 Alt	β_0 Null	β_1 Min. Theo.	β_1 Alt	β_1 Null	β_2 Min. Theo.	β_2 Alt	β_2 Null	ϑ Min. Theo.	ϑ Alt	ϑ Null	σ^2 Min. Theo.	σ^2 Alt	σ^2 Null
GM	0.0006	0.0006	0.0005	3E-06	3.19E-06	3.19E-06	0.0009	0.00090	0	1E-04	1E-04	0.0002	5E-06	4.5E-06	4.5E-06
WM	0.0006	0.0006	0.0005	3E-06	3.2E-06	3.2E-06	0.0009	0.00090	0	1E-04	1E-04	0.0002	5E-06	4.5E-06	4.5E-06
CSF	0.0006	0.0006	0.0005	3E-06	3.19E-06	3.18E-06	0.0009	0.00090	0	1E-04	1E-04	0.0002	5E-06	4.5E-06	4.5E-06
Out	0.0006	0.0008	0.0006	3E-06	4.12E-06	4.13E-06	0.0009	0.00117	0	4E+10	0.907	0.9015	5E-06	4.5E-06	4.5E-06
ROI	0.0006	0.0006	0.0005	3E-06	3.2E-06	3.2E-06	0.0009	0.00090	0	1E-04	1E-04	0.0002	5E-06	4.5E-06	5.7E-05

Table 4. The average voxel values of the MO Model mean maps.

MEAN	β_0			β_1			β_2			σ^2		
	β_0 True	β_0 Alt	β_0 Null	β_1 True	β_1 Alt	β_1 Null	β_2 True	β_2 Alt	β_2 Null	σ^2 True	σ^2 Alt	σ^2 Null
GM	2.708	2.708	2.708	0.01	0.0100	0.01000	2.047E-16	-1.6E-06	0	0.0001	9.938E-05	9.96E-05
WM	2.758	2.758	2.758	0.01	0.0100	0.01000	2.1858E-16	-1E-06	0	0.0001	9.934E-05	9.95E-05
CSF	2.757	2.757	2.757	0.01	0.0100	0.01000	3.3307E-16	-3.4E-06	0	0.0001	9.936E-05	9.96E-05
Out	0.000	0.013	0.013	1E-17	0.0000	0.00000	6.163E-31	2.98E-07	0	0.0001	4.266E-05	4.27E-05

ROI	2.708	2.708	2.832	0.01	0.0100	0.00998	0.25421653	0.254215	0	0.0001	9.941E-05	0.016244
-----	-------	-------	--------------	------	--------	---------	------------	----------	---	--------	-----------	-----------------

Table 5. The average voxel values of the MO Model standard deviation maps.

SD	β_0			β_1			β_2			σ^2		
	β_0 Min. Theo.	β_0 Alt	β_0 Null	β_1 Min. Theo.	β_1 Alt	β_1 Null	β_2 Min. Theo.	β_2 Alt	β_2 Null	σ^2 Min. Theo.	σ^2 Alt	σ^2 Null
GM	0.0006	6E-04	0.0005	3E-06	3E-06	3.19E-06	0.000904	0.000904	0	6E-06	6.369E-06	6.38E-06
WM	0.0006	6E-04	0.0005	3E-06	3E-06	3.2E-06	0.000904	0.000904	0	6E-06	6.357E-06	6.36E-06
CSF	0.0006	6E-04	0.0005	3E-06	3E-06	3.18E-06	0.000904	0.000904	0	6E-06	6.358E-06	6.36E-06
Out	0.0006	4E-04	0.0003	3E-06	2E-06	2.09E-06	0.000904	0.000592	0	6E-06	2.894E-06	2.9E-06
ROI	0.0006	6E-04	0.0005	3E-06	3E-06	3.2E-06	0.000904	0.000905	0	6E-06	6.364E-06	0.000115

Table 6. The average voxel values of the DeTeCT Model mean maps.

MEAN	M_0			T_1			T_2^*			δ		
	M_0 True	M_0 Alt	M_0 Null	T_1 True	T_1 Alt	T_1 Null	T_2^* True	T_2^* Alt	T_2^* Null	δ True	δ Alt	δ Null
GM	0.83	0.834	0.833	1.331	1.327	1.327	0.042	0.0426	0.0425	0	7.37E-06	0
WM	0.71	0.711	0.711	0.832	0.830	0.830	0.049	0.0495	0.0495	0	6.74E-06	0
CSF	1	1.030	1.025	4	4.025	4.021	2.2	9.6711	14.079	0	1.317	0
Out	1E-11	0.0004	0.0006	1000	1001.76	1001.88	1000	773.346	921.512	1E-17	-57.17	0
ROI	0.83	0.8563	9.446	1.331	1.3205	0.0783	0.042	0.0407	0.0120	1	3.8058	0

	β_1			ϑ			σ^2		
	β_1 True	β_1 Alt	β_1 Null	ϑ True	ϑ Alt	ϑ Null	σ^2 True	σ^2 Alt	σ^2 Null
GM	0.01	0.0100	0.0100	0.7853	0.7853	0.7853	0.0001	9.95E-05	9.96E-05
WM	0.01	0.0099	0.0099	0.7853	0.7853	0.7853	0.0001	9.94E-05	9.95E-05
CSF	0.01	0.0099	0.0099	0.7853	0.7853	0.7853	0.0001	9.95E-05	9.96E-05
Out	1E-17	-3.48E-09	-3.50E-09	0	0.0004	0.0004	0.0001	9.96E-05	9.96E-05
ROI	0.01	0.0099	0.0100	0.7853	0.7853	0.7853	0.0001	9.95E-05	0.008020

Table 7. The average voxel values of the DeTeCT Model standard deviation maps.

SD	M_0			T_1			T_2^*			δ		
	M_0 Min. Theo.	M_0 Alt	M_0 Null	T_1 Min. Theo.	T_1 Alt	T_1 Null	T_2^* Min. Theo.	T_2^* Alt	T_2^* Null	δ Min. Theo.	δ Alt	δ Null
GM	0.0857	0.0856	0.0851	0.0358	0.0367	0.0365	0.0052	0.0055	0.0054	0.00023	0.000253	0
WM	0.0537	0.0537	0.0534	0.0237	0.0240	0.0238	0.0053	0.0055	0.0054	0.00024	0.000259	0

CSF	0.0718	0.8674	0.1191	0.0158	3.9971	0.5101	8.8591	20.285	25.833	0.46598	24.77650	0
Out	0.2807	1.1572	4.3318	3.14E-13	74.257	75.814	1.14E-19	7140.6	1203.4	5.65E-20	5053.601	0
ROI	0.0857	0.0586	3.0724	0.0358	<i>0.0370</i>	<i>0.0271</i>	0.0052	0.0029	0.0020	3.2462	6.813494	0
	β_1				ϑ					σ^2		
	β_1 Min. Theo.	β_1 Alt	β_1 Null		ϑ Min. Theo.	ϑ Alt	ϑ Null			σ^2 Min. Theo.	σ^2 Alt	σ^2 Null
GM	3.08E-06	3.08E-06	3.08E-06		1.44E-04	1.44E-04	1.44E-04			4.43E-06	4.41E-06	4.42E-06
WM	3.08E-06	3.08E-06	3.08E-06		1.42E-04	1.42E-04	1.42E-04			4.43E-06	4.41E-06	4.41E-06
CSF	3.08E-06	3.03E-06	3.03E-06		1.41E-04	1.41E-04	1.41E-04			4.43E-06	4.42E-06	4.43E-06
Out	9.54E-07	3.91E-06	3.91E-06		6.72E-12	8.33E-01	8.32E-01			4.43E-06	4.42E-06	4.42E-06
ROI	3.08E-06	3.05E-06	3.68E-06		1.38E-04	1.38E-04	1.39E-04			4.43E-06	4.41E-06	5.63E-05

Table 8. The average voxel values of the DeTeCT-ING Model mean maps.

MEAN	M_0			δ			β_1			ϑ			σ^2		
	M_0 True	M_0 Alt	M_0 Null	δ True	δ Alt	δ Null	β_1 True	β_1 Alt	β_1 Null	ϑ True	ϑ Alt	ϑ Null	σ^2 True	σ^2 Alt	σ^2 Null
GM	0.83	0.8299	0.829	0	1.18E-06	0	0.01	0.0100	0.0100	0.7853	0.7853	0.7853	0.0001	9.96E-05	9.97E-05
WM	0.71	1.0801	1.079	0	- 2.44E-05	0	0.01	0.0099	0.0099	0.7853	0.7853	0.7853	0.0001	9.98E-05	9.99E-05
CSF	1	1.0881	1.086	0	- 0.00019	0	0.01	0.0099	0.0099	0.7853	0.7853	0.7853	0.0001	0.000112	0.000112
Out	1E-11	1.91E-06	3.79E-06	1E-17	45.1519	0	1E-17	- 2.83E-09	- 3.26E-09	0	0.0001	0.0002	0.0001	9.95E-05	9.96E-05
ROI	0.83	0.8300	1.382	1	1.0169	0	0.01	0.0099	0.0100	0.7853	0.7853	0.7853	0.0001	9.96E-05	0.008096

Table 9. The average voxel values of the DeTeCT-ING Model standard deviation maps.

SD	M_0			δ			β_1			ϑ			σ^2		
	M_0 Min. Theo.	M_0 Alt	M_0 Null	δ Min. Theo.	δ Alt	δ Null	β_1 Min. Theo.	β_1 Alt	β_1 Null	ϑ Min. Theo.	ϑ Alt	ϑ Null	σ^2 Min. Theo.	σ^2 Alt	σ^2 Null
GM	0.0857	0.004836	0.004430	0.000233	0.000232	0.000000	0.000000	0.000000	0.000000	0.000144	0.000144	0.000144	0.000000	0.000000	0.000000
WM	0.0537	0.004828	0.004427	0.000244	0.000178	0.000000	0.000000	0.000000	0.000000	0.000144	0.000144	0.000144	0.000000	0.000000	0.000000
CSF	0.0718	0.004829	0.004420	0.492673	0.000176	0.000000	0.000000	0.000000	0.000000	0.000144	0.000144	0.000144	0.000000	0.000000	0.000000

Out	0.2807	0.00637 4	0.00587 9	0.00000 0	709.298	0.00000 0	0.00000 1	0.00000 4	0.00000 4	0.00000 0	0.83754 3	0.85797 5	0.00000 4	0.00000 4	0.00000 4
ROI	0.0857	0.00481 2	0.00441 8	3.24621 2	0.13642 6	0.00000 0	0.00000 3	0.00000 3	0.00000 3	0.00013 8	0.00013 8	0.00013 9	0.00000 4	0.00000 4	0.00005 6

For the quantitative analysis of the activation detection performances of the models, the simulation results presented in Part II of Section 3.1 were evaluated by utilizing three criteria. The first two are the true positive rate (TPR), proportion of the times that an active is correctly detected as active, and false positive rate (FPR), proportion of the times that an inactive voxel is incorrectly detected as active. The third criterion is the receiver operator characteristic (ROC), which is a plot FPR (one minus the specificity) on the x -axis versus TPR (sensitivity) on the y -axis, which gives the tradeoff between the cost of failing to detect the activity against the cost of raising false positives. For the first two criteria, we generate the TPR and FPR versus the parameters varied, δ and α , curves for Scenarios “a” and “b”, respectively, introduced in Part II of Section 3.1. For the ROC curves, each varying parameter value (δ or α) determines a (x, y) point on the curve. To generate the ROC curves for Scenarios “a” and “b”, TPR and FPR for a fixed δ or α value are computed from the data of the selected active and inactive voxels, respectively. These are then averaged across 1000 simulated images to generate the (x, y) point. This is repeated for the considered range of the varied parameter values to generate a curve. ROC curves range from $(0, 0)$ to $(1, 1)$, and a good model is ideally expected to have a curve that is as close to the upper left quadrant $(1, 0)$ as possible.

In order to better evaluate the efficiency of the models’ estimators, the single voxel simulation that is performed under Scenario “a” is used for the analyses of the properties of the parameter estimates. The first criterion of such analysis is to compare the computed CRLBs and the sample variances of the parameters at varying δ , whereas the second criterion is to compare mean squared errors (MSEs) of the estimators, which incorporate both the variance and the bias of the estimators, at varying δ .

All computations were performed on an HP Z600 with dual-quad core Xeon X5570 2.93 GHz processors, 24 GB of DDR3 RAM, 1 TB SATA-300 hard drive, 64 bit, Windows 7 in Matlab 2012. The computation times of the DeTeCT and DeTeCT-ING Models for the estimation of the model parameters and the activation statistics of a 96×96 human subject data that were acquired with the setting given in Section 3.2 were found to be 77.36 min and 9.23 min, respectively. The reason for having a higher computation time for the DeTeCT Model can be explained by the computational complexity of this model resulting from simultaneous estimation of seven parameters.

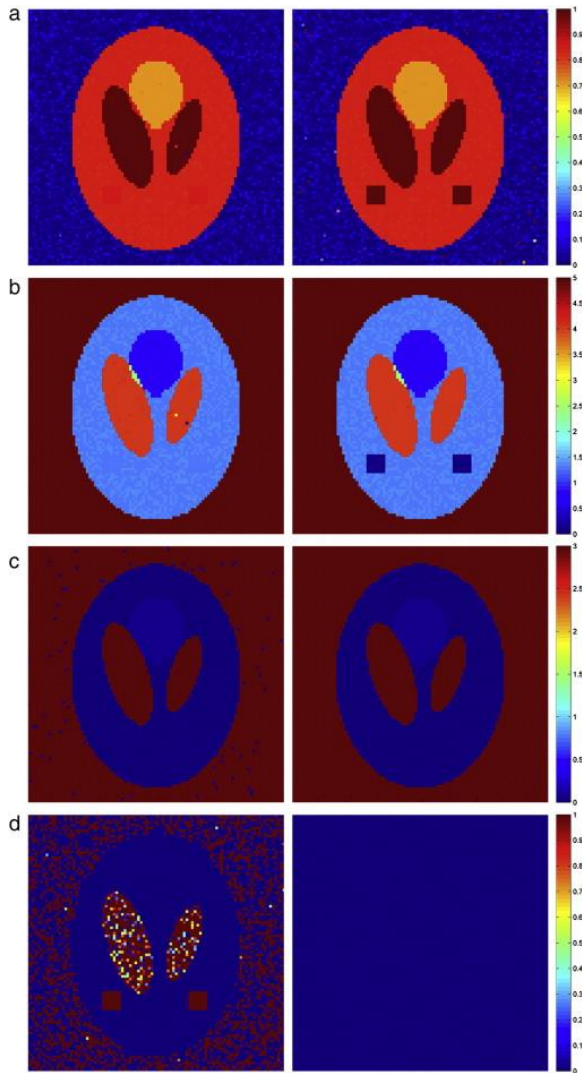
4.2. Simulated Data Results

4.2.1. Part I: Simulated Phantom Data with the Fixed Parameter Setting

The true value and the theoretical minimum standard deviation maps of the parameters of the CV and MO Models were produced according to MLEs and CLRBS of the model by using the noiseless complex fMRI data [20], [26]. The average voxel values of the true values as well as the calculated sample mean maps of the estimated parameters under the null and alternative hypothesis for each tissue type are given in Table 2 for CV Model, and in Table 4 for MO Model. Similar tables for the theoretical minimum and computed sample standard deviation maps of the CV and MO Models are also given in Table 3, Table 5, respectively. It can be observed that CV and MO Models mostly yield “good” results. However, it should be noted here that the results of these two models are compared with the true value and theoretical minimum standard deviation maps calculated from the considered models themselves. Furthermore, the CV and MO Models do not provide the proton spin density and relaxation parameter estimates unlike the DeTeCT and DeTeCT-ING Models.

The true parameter maps of the DeTeCT and DeTeCT-ING Models are given in Fig. 2(a)–(f). The calculated sample mean of the estimated parameters, M_0 , T_1 , T_2^* , δ , β_1 , ϑ , σ^2 , from the DeTeCT Model are given in Fig. 4(a)–(g) (left: alternative, right: null hypothesis), respectively. It can be observed that the estimated parameters under the alternative hypothesis appear to be similar to the true parameter values given in Fig. 1 except for the blurring that is the result of the noise in the signal as well as the systematic error of the numerical optimization procedure. It can also be seen that the most apparent difference between the null and alternative hypotheses estimation results occurs in ROIs which become especially significant in M_0 , T_1 , δ , and σ^2 results given in Fig. 4(a),

(b), (d) and (g) since the only difference in the hypothesis setting given in Eq. (21) occurs in ROIs. Table 6 provides a better comparison between the true value and the sample mean estimated parameter values. One can observe that the difference between the calculated sample means of the parameters such as T_2^* and δ is higher compared to the difference for the other parameters in GM tissue and outside brain. The poor estimation that appears in such tissues could be considered as the result of having a nonlinear objective function given in Eq. (19) and six different parameters to be optimized in this system. Table 7 illustrates a comparison between the theoretical minimum standard deviations of the parameters that were calculated according to the numerically calculated CRLBs and the computed sample standard deviations of the estimated parameters. Although the sample standard deviations of T_2^* and δ are higher compared to the related CRLBs, the DeTeCT Model mostly produces “good” results in terms of the variances of the estimated parameters.



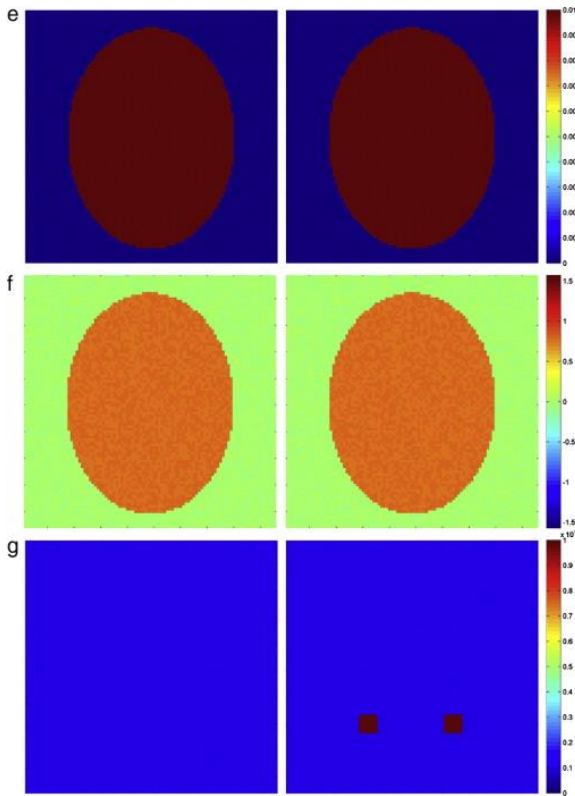


Fig. 4. Calculated sample mean maps of the DeTeCT Model parameters. a) $\mu(\hat{M}_0)$ and $\mu(\check{M}_0)$, b) $\mu(\hat{T}_1)$ and $\mu(\check{T}_1)$ in s., c) $\mu(\hat{T}_2^*)$ and $\mu(\check{T}_2^*)$ in s., d) $\mu(\hat{\delta})$ and $\mu(\check{\delta})$, e) $\mu(\hat{\beta}_1)$ and $\mu(\check{\beta}_1)$, (f) $\mu(\hat{\vartheta})$ and $\mu(\check{\vartheta})$, g) $\mu(\hat{\sigma}^2)$ and $\mu(\check{\sigma}^2)$.

The sample mean of the estimated parameters, M_0 , δ , β_1 , ϑ , and σ^2 , of the DeTeCT-ING Model under the null and alternative hypotheses is shown in Fig. 5(a)–(e) (left: alternative, right: null hypothesis), respectively. The average voxel values of the true parameter values and the calculated sample mean maps are given in Table 8 whereas the CRLBs and the calculated sample standard deviations are shown in Table 9. Fig. 5 as well as Table 7, Table 8 show that the DeTeCT-ING Model has a high statistical power in estimating the parameters. One can observe that the only “fair” and “poor” estimates appear to be in WM M_0 and δ outside the phantom. However, better δ estimates can be seen in Fig. 5(b) compared to Fig. 4(d). It should be noted here that no signal areas, such as outside of the brain, have not been masked after estimation. It is thus expected that the parameters for the voxels outside the phantom may not have been estimated precisely as we expect.

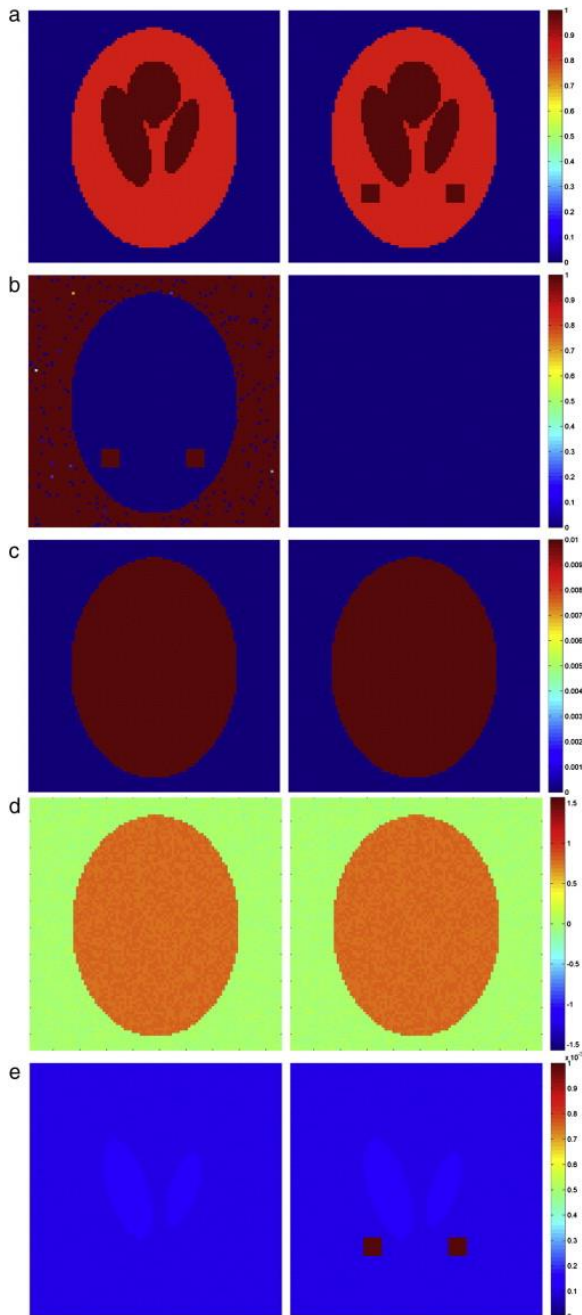


Fig. 5. Calculated sample mean maps of the DeTeCT-ING Model parameters. a) $\mu(\hat{M}_0)$ and $\mu(\tilde{M}_0)$, b) $\mu(\hat{\delta})$ and $\mu(\tilde{\delta})$, c) $\mu(\hat{\beta}_1)$ and $\mu(\tilde{\beta}_1)$, (d) $\mu(\hat{\sigma}^2)$ and $\mu(\tilde{\sigma}^2)$, e) $\mu(\hat{\sigma}^2)$ and $\mu(\tilde{\sigma}^2)$.

As previously noted, activations are calculated from the likelihood ratio statistics $-2\log\lambda_M$ for MO Model and $-2\log\lambda_C$ for CV, DeTeCT, and DeTeCT-ING Models given in Eqs. (9), (15). The sample mean and the standard deviation of the activation statistics maps, Z-statistics for CV, DeTeCT and DeTeCT-ING Models and t -statistics for MO Model, which were thresholded at a 5% Bonferroni family-wise error rate are given in Fig. 6(a)–(d) and (e)–(h), respectively. None of the models appears to produce false positives due to the low uncertainty in the simulated data. However, Fig. 6(e)–(h) shows that DeTeCT-ING Model produces lower variance in all tissue types in the phantom compared to the other models.

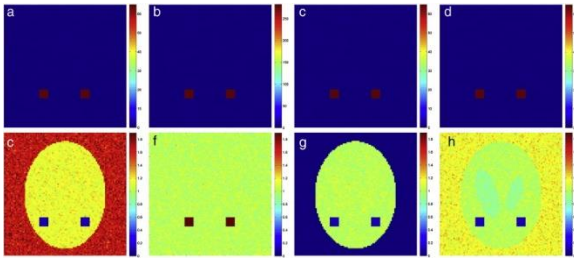


Fig. 6. First row: Calculated sample means of the activation statistics (Z or t) of the models. a) $\mu(Z)$ (CV Model), b) $\mu(t)$ (MO Model), c) $\mu(Z)$ (DeTeCT Model), d) $\mu(Z)$ (DeTeCT-ING Model) Second row: Calculated sample standard deviations of the activation statistics (Z or t) of the models. e) $\mu(Z)$ (CV Model), f) $\mu(t)$ (MO Model), g) $\mu(Z)$ (DeTeCT Model), h) $\mu(Z)$ (DeTeCT-ING Model).

We give a comparison between the CRLBs, which provide a quantitative measure of the attainable precision of parameter estimates, of the considered models in Table 10, Table 11. It can be observed from Table 10 and the results of a previous study [26] that the CRLB for the variance of the estimate of the observation variance is two times larger in the MO model than in the CV model. Table 11 shows that the CRLBs of the estimates of the common parameters of the DeTeCT and DeTeCT-ING Models are the same since these models have the same likelihood functions. It can also be seen from Table 10, Table 11 that the common parameters of all four models such as β_1 and ϑ appear to have the same CRLBs. The minimal theoretical standard deviations of the estimates of M_0 , T_1 and T_2^* are higher compared to those of the other parameters. The DeTeCT and DeTeCT-ING Models appear to have higher CRLBs of the estimate of δ in CSF and ROI areas compared to the other areas. It should be noted here that the CRLBs of MO and CV Models and the DeTeCT and DeTeCT-ING Models are not based on the same number of TRs since the first 20 observations are excluded for MO and CV Models.

Table 10. Minimal theoretical standard deviation values of the CV and MO Model parameters.

<i>SD</i>	<i>MO</i>				<i>CV</i>				
	θ_0	θ_1	θ_2	σ^2	θ_0	θ_1	θ_2	ϑ	σ^2
GM	0.0006	3E-06	0.0009	6E-06	0.0006	3E-06	0.0009	1E-04	5E-06
WM	0.0006	3E-06	0.0009	6E-06	0.0006	3E-06	0.0009	1E-04	5E-06
CSF	0.0006	3E-06	0.0009	6E-06	0.0006	3E-06	0.0009	1E-04	5E-06
Out	0.0006	3E-06	0.0009	6E-06	0.0006	3E-06	0.0009	4E + 10	5E-06
ROI	0.0006	3E-06	0.0009	6E-06	0.0006	3E-06	0.0009	1E-04	5E-06

Table 11. Minimal theoretical standard deviation values of the DeTeCT and DeTeCT-ING Model parameters.

<i>SD</i>	<i>DeTeCT</i>				<i>DeTeCT-ING</i>							
	M_0	T_1	T_2^*	δ	θ_1	ϑ	σ^2	M_0	δ	θ_1	ϑ	σ^2
GM	0.0857	0.0358	0.0052	0.00023	3.08E-06	1.44E-04	4.43E-06	0.0857	0.000233	3.08E-06	1.44E-04	4.43E-06
WM	0.0537	0.0237	0.0053	0.00024	3.08E-06	1.42E-04	4.43E-06	0.0537	0.000244	3.08E-06	1.42E-04	4.43E-06
CSF	0.0718	0.0158	8.8591	0.46598	3.08E-06	1.41E-04	4.43E-06	0.0718	0.492673	3.08E-06	1.41E-04	4.43E-06
Out	0.2807	3E-13	1.14E-19	5.65E-20	9.54E-07	6.72E-12	4.43E-06	0.2807	0.000000	9.54E-07	6.72E-12	4.43E-06
ROI	0.0857	0.0358	0.0052	3.2462	3.08E-06	1.38E-04	4.43E-06	0.0857	3.246212	3.08E-06	1.38E-04	4.43E-06

4.2.2. Part II: Simulated Data of Two Voxels with the Varying Parameter Setting

Figs. 7(a), (b) and 8(a), (b) illustrate the TPR and FPR plots against the varied parameter, δ and α under Scenarios “a” and “b”, respectively. Furthermore, Fig. 8c shows the ROC curves plotted while α is varied under Scenario “b”. ROC curve at varying δ is not presented because the FPR computed from the inactive voxel is not affected by the varying parameter, δ , as it is zero for the inactive voxel. In the plots presented in Fig. 7, Fig. 8, the colors red, green, blue and black represent the models CV, MO, DeTeCT and DeTeCT-ING, respectively.

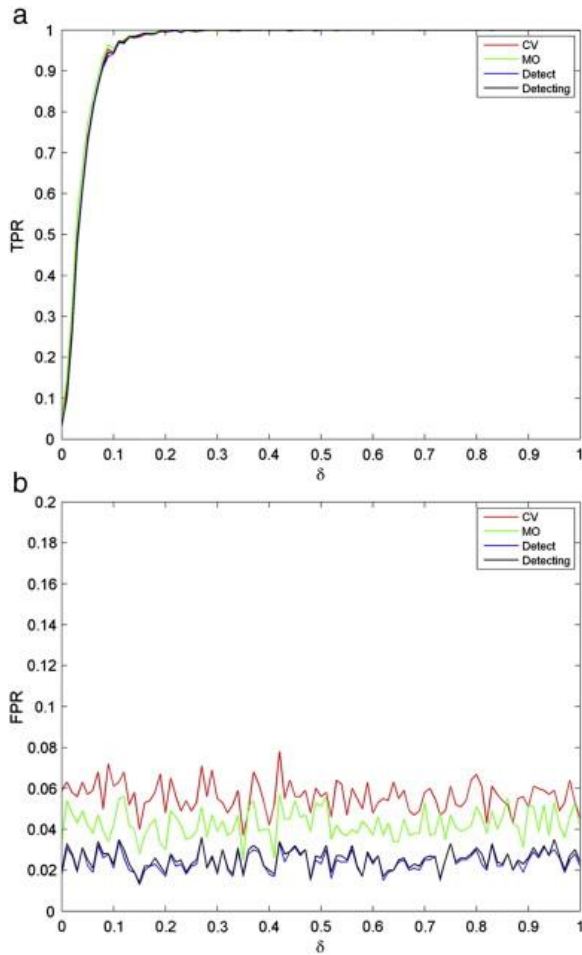


Fig. 7. (a) TPR and (b) FPR plots against the varied parameter, δ , under Scenario “a” in which $\sigma = 0.5$, and $\alpha = 0.05$.

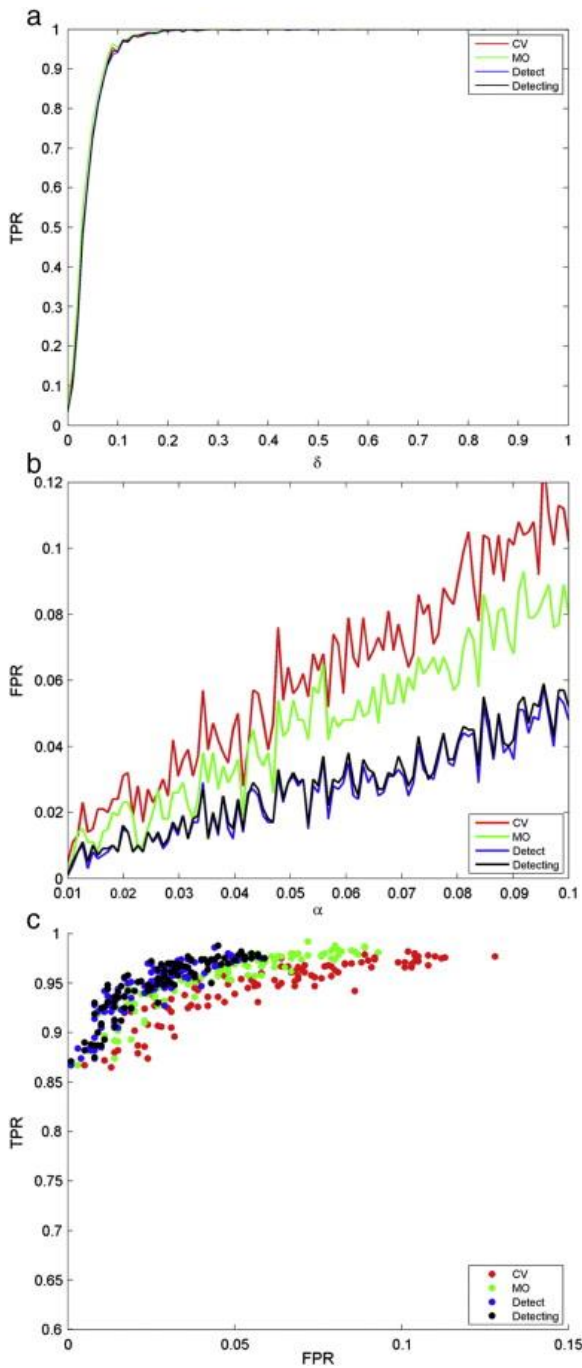


Fig. 8. (a) TPR, (b) FPR plots against the varied parameter, α , and (c) ROC curve under Scenario “b” in which $\sigma = 0.5$, and $\delta = 0.1$.

Fig. 7(a) and (b) shows the plots of TPR and FPRs for each model against δ for an $\alpha = 0.05$ significance level, which are based on 1000 simulated time series with $\sigma = 0.5$. As seen in Fig. 7(a), even though TPRs of the models seem to coincide with each other; the MO and CV models have slightly higher TPRs especially at low δ values. However, there seems to be a trade-off between the TPRs and FPRs of the CV and MO Models, as Fig. 7(b) shows that FPRs of the CV and MO models are also higher than the DeTeCT and DeTeCT-ING Models’ FPRs. This may be explained by the fact that our simulations are based on the data generated from Eq. (17) which is closer to the physical magnetization of the signal than the linear model that the MO and CV models use. One can observe that the FPRs of the DeTeCT and DeTeCT-ING Models do not converge to the significance level of $\alpha =$

0.05 in Fig. 7(b), possibly due to some kind of bias that might have been created during the nonlinear numerical optimization process.

Fig. 8(a)–(c) shows the plots of TPR and FPRs for each model against significance level, α , as well as the ROC scatter plot generated at varying α for $\delta = 0.1$ for the active voxel, which are based on 1000 simulated time series with $\sigma = 0.5$. TPR plots of the CV, DeTeCT and DeTeCT-ING Models seem to slightly differ from each other whereas the MO model has insignificantly higher TPRs at almost all α values. As expected, it can be observed in Fig. 8(b) that the FPRs of the models increase with significance level, α . Moreover, the DeTeCT and DeTeCT-ING Models show lower FPRs than the MO and CV Models at all α levels. ROC scatter plots in Fig. 8(c) show the full picture of trade-off between the TPR and FPR across a series of α values. Since more accurate activation detection model is expected to have a closer ROC curve to the upper-left border of the ROC space, the DeTeCT and DeTeCT-ING Models can be observed to be more accurate as producing less trade-off between FPR and TPRs. It can also be seen in Fig. 8(c) that the FPRs of the DeTeCT and DeTeCT-ING Models are not as high as the ones of MO and CV models at any significance level, α .

Fig. 9 shows the plots of CRLBs and sample variances of the models' parameters against δ for the single active voxel data generated based on Scenario "c" in which $\alpha = 0.05$, $\sigma = 0.01$ and δ varying from 0 to 1 with increments of 0.1. Since the CV and MO models do not include M_0 , T_1 , T_2^* and δ ; the MO model does not include θ ; and the DeTeCT and DeTeCT-ING models do not include β_0 and β_2 , the corresponding panels of Fig. 9 do not include such parameters. Further, Fig. 10 shows the plots of sample means and MSEs of the estimated σ^2 's under each model against δ that are computed from the same single voxel data generated under Scenario "c". We prefer to present the MSE plots of the parameter σ^2 only since the MSEs of the other parameters are significantly close to the variance plots presented in Fig. 9 as a result of low bias of the estimators. In the plots presented in Fig. 9, Fig. 10, the colors red, green, blue and black represent the sample variances, MSEs or sample means of the CV, MO, DeTeCT and DeTeCT-ING models, whereas in Fig. 9, pink, cyan, and yellow represent the CRLBs of the CV, MO, and DeTeCT/DeTeCT-ING models, respectively. As noted before, the DeTeCT and DeTeCT-ING Models have the same CRLBs since these models have the same likelihood functions.

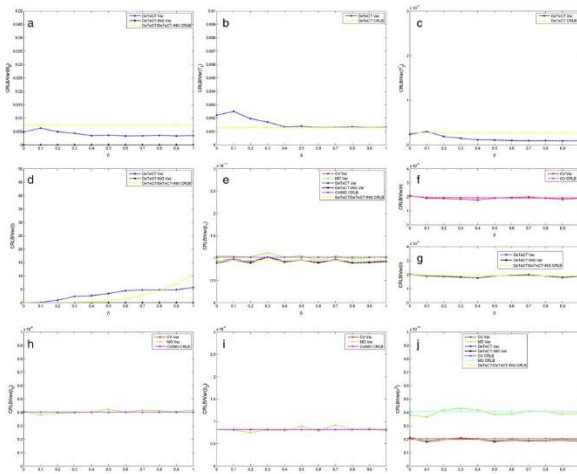


Fig. 9. CRLB and sample variance plots of the parameters against δ for the single active voxel data generated based on Scenario "c" in which $\alpha = 0.05$, $\sigma = 0.01$. a) M_0 , b) T_1 , c) T_2^* , d) δ , e) β_1 , f) θ , g) β_0 , h) β_2 , and i) σ^2 .

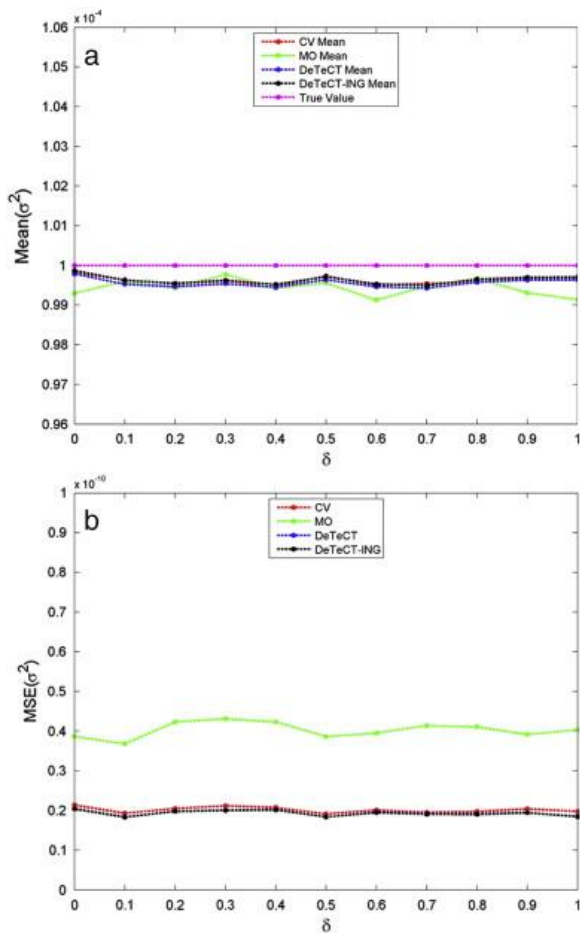


Fig. 10. (a) Sample mean, and (b) MSE plots of σ^2 against δ for the single active voxel data generated based on Scenario “c” in which $\alpha = 0.05$, $\sigma = 0.01$.

It can be seen in Fig. 9(a), (c) and (d) that the sample variances of the estimated M_0 , T_2^* and δ for the DeTeCT model (in blue) appear to be close but not coincident to the CRLB values (in yellow) whereas the sample variances of the estimated M_0 and δ for the DeTeCT-ING model (in black) can be observed to be lower than CLRBS (in yellow) at all δ values. The sample variance plot of the estimated T_1 that is given in Fig. 9(b) appears to coincide with its CRLB at α values higher than 0.4. It can be seen in Fig. 9e that the variances of β_1 for all models achieve their CRLBs. It should be noted here that the DeTeCT and DeTeCT-ING models’ CRLBs (yellow) are lower than the CV and MO models’ CRLBs (pink) for the coefficient β_1 . In Fig. 9(f) and (g), the variance of θ appears to achieve its CRLBs for all models considered. Further, the variances of the coefficients β_0 and β_2 for the CV and MO models (in red and yellow), presented in Fig. 9(h) and (i), appear to achieve their CRLBs (in pink). Error variance estimate, given in Fig. 9(j), is approximately twice as large for the MO model than for the CV, DeTeCT and DeTeCT-ING models. This observation was verified by the fact that the CRLB for the variance of the observation variance is two times larger in the magnitude only data than the complex-valued data [26]. As such, the CRLBs for the variance of σ^2 in the DeTeCT and DeTeCT-ING models are also found to be very close to the CRLBs for the variance of σ^2 in CV model. Furthermore, the estimated variances of all models appear to be very close to their corresponding CRLBs.

In Fig. 10(a), we present the computed sample means of σ^2 for all models as well as the true σ^2 value that we used when generating the data. Furthermore, we present the MSEs of σ^2 for the models at varying δ in Fig. 10(b). It can be observed in Fig 10(a) that the sample means of σ^2 computed from the CV, DeTeCT and DeTeCT-ING models appear to be very close to each other and also to the true σ^2 value. MO model seems to

produce a lower error compared to the other models mostly at higher δ points. However, as a result of the MO model's higher minimal theoretical error variance, the MSE of σ^2 for the MO model appears to be higher than the other models, as it can be seen in Fig. 10(b). Further, the DeTeCT and DeTeCT-ING models seem to have slightly lower MSEs for σ^2 than the CV model. Since the MSE decomposes into a sum of the bias and variance of the estimator, the MSE of the estimators needs to be as small as possible in order to achieve a good estimation performance.

In general, the parameter estimates for the CV, DeTeCT and DeTeCT-ING models appear to be more efficient than the MO model at the considered δ levels. It should also be noted here that the DeTeCT and DeTeCT-ING models have superior benefits than the CV and MO models in terms of extracting more information from fMRI data by providing M_0 , T_1 and T_2^* estimates as well as activation detection. Lower variance and bias of the variance estimator, σ^2 imply a more stable variance of the model. Furthermore, lower mean of the variance estimator σ^2 provides better stability of the other parameter estimates since the CRLBs of all estimators depend on σ^2 . As such, a better accuracy and stability of the DeTeCT and DeTeCT-ING Models can lead to better activation detection by providing lower FPRs, higher TPRs and ROC curves closer to the left quadrant, especially at extreme situations such as at low δ and very low or high α levels.

4.3. Human Subject Data Results

Data acquired for a human subject are corrupted by noise as a result of physiological effects and possible motion. Nonlinearity and the number of the parameters to be estimated in the system as well as the noise in the acquired data may pose computational difficulty when performing the nonlinear LS estimation. However, such problem can be overcome by choosing reasonable initial values of the parameters for the iterative search. In order to develop a more hybrid approach to the nonlinear estimation, the MLEs of M_0 , β_1 , and ϑ were analytically driven under the restricted null hypothesis of the DeTeCT-ING Model to be used as initial values. The derivations of the MLEs of the null hypothesis of the DeTeCT-ING Model are given in Appendix B.

The tissue parameter maps, M_0 , T_1 , and T_2^* , estimated from the alternative hypothesis of the DeTeCT Model given in Eq. (21) by using the numerical nonlinear are shown in Fig. 11(a)–(c). Fig. 12(a)–(c) shows activation images using the likelihood ratio test from the CV, MO and DeTeCT-ING Models, respectively. It can be observed that M_0 , T_1 , and T_2^* values are highly indicative of GM bordered in Fig. 11(a)–(c). Fig. 12 shows a high correspondence between decay coefficients deemed to be GM and bordered active areas that should be in GM. It can be observed that GM T_1 values are higher than WM T_1 values as it is given in Table 1. Corresponding tissues can also be seen in T_2^* map in Fig. 11(c). It is evident that the CV and DeTeCT-ING Models demonstrate superior power of detection over the MO model in left motor cortex and supplementary motor area in which the activation occurs. A higher power of detection can be seen in the bordered left motor cortex in Fig. 12(c) compared to the corresponding areas in Fig. 12(a) and (b). This observation is consistent with the outcomes of our simulation study presented in Fig. 8 in Part II of Section 4.2 which shows that the DeTeCT-ING model has a better activation detection power than the CV and MO models. Fig. 12(c) also shows that the DeTeCT-ING model produces no false positives outside brain unlike the CV model. Even though the false positive detections of this kind, which are distant from the tissues, can be easily masked, this outcome can be considered as the evidence of the DeTeCT-ING model's benefit of theoretically eliminating false positive rates without the need of researchers' decision for manual masking after the statistical analysis of the observed fMRI data. A few false positives that are not present in the CV or MO models can also be observed in the upper left side of the brain which is very close to no signal area. Such false positives can be caused by the signal changes due to non-uniform sources of noise and artifact that are hard to be described and modeled. Furthermore, the assumption of independence of the observations in time or space may not be true in the human subject data. Such assumptions that are difficult to be satisfied can cause poor estimates and thus false positive rates especially in

the areas near the edges of the brain. As such, these voxels that are incorrectly detected as active most possibly have task related signal changes that are not of biological origin.

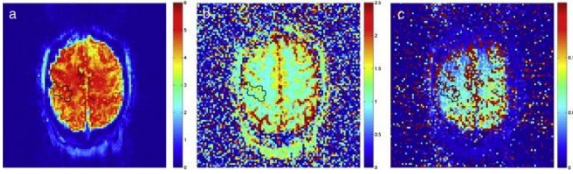


Fig.11. Estimated M_0 , T_1 , and T_2^* maps from the alternative hypothesis of the DeTeCT Model. a) M_0 , b) T_1 (in s.), c) T_2^* (in s.).

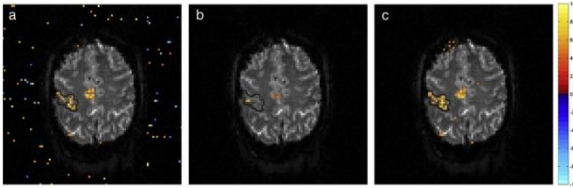


Fig. 12. Activation images thresholded at 5% FWE rate from a) CV, b) MO, and c) DeTeCT-ING Models.

5. Discussion

This work proposes a new statistical fMRI model for differential T_2^* contrast, so called the DeTeCT-ING Model, by incorporating T_1 and T_2^* of gray matter tissue, considering the fact that the active voxels are located in gray matter. Furthermore, the physical magnetization equation was included into the model rather than using a linear model to describe the magnetization. Unlike the previously presented fMRI activation models, the first scans of fMRI data were not discarded since they have the biological information of the brain, including the tissue parameters such as relaxation parameter and spin density of the tissues.

The selection of the imaging parameters, TR, TE and flip angle, plays an important role for determining accurate measure of tissue parameters. The acquisition parameters for this study were selected to be appropriate for both T_1 and T_2^* estimation and brain activation detection since we perform them from a single pulse sequence. The selection of 90° flip angle was made in order to simplify the temporarily varying magnitude M_t , given in Eq. (17) so that the magnetization at time for the DeTeCT and DeTeCT-ING Models does not depend on the magnetization at previous time point. As such, the computational complexity of the numerical optimization of the log likelihood function is relatively reduced. It should be noted here that it is possible to reduce TR and TE to increase T_1 and T_2^* contrast since T_1 and T_2^* are influenced by TR and TE, respectively. Discarding the computational complexity of the problem, the optimum flip angle that can give the optimum T_1 and T_2^* estimates in terms of the accuracy of the measurements would be the one that makes the signal weighted equally on T_1 and T_2^* .

There are three main contributions of the developed model to the current studies in the field by utilizing the aforementioned neglected information. First, the proposed method provides a significant step to modeling the fMRI data closer to that actually seen in the real experiments with the use of physical magnetization equation. Second, utilization of the gray matter tissue relaxation parameters in the statistical fMRI activation model provides a theoretical elimination of the possible false positives in the process of hypothesis testing while computing activation statistics. As such, the DeTeCT-ING Model provides more accurate and significant activation statistics. Third, the model allows one to simultaneously estimate the relaxation parameters which could be used for tissue characterization, by utilizing the information in the first few images.

The proposed model in this study can be applied to improve the sensitivity to detect brain activation in fMRI by theoretically restricting the search volume of the statistical analysis to the grey matter only. The primary application of the method can be fMRI analysis for the diagnosis of grey matter diseases such as degenerative diseases by automatically segmenting grey matter to limit analysis to grey matter voxels. The method can be useful in the analysis of fMRI data that are prone to produce false positive rates as a result of thermal noise, physiological noise, or correlated noise in the data.

Appendix A. CRLBs of the DeTeCT and DeTeCT-ING Models

The CRLB for the variance of an unbiased estimate of a model parameter requires the second derivatives of the logarithm of the likelihood function, LL , with respect to the model parameters. The logarithm of the likelihood function of the DeTeCT and DeTeCT-ING Models can be written as

(A.1)

$$LL = -n \log(2\pi) - \sum_{t=1}^n \log r_t - n \log \sigma^2 - \frac{1}{2\sigma^2} \sum_{t=1}^n [r_t^2 + M_t^2 - 2M_t^2 - 2M_t r_t \cos(\phi - \theta)]$$

where the temporarily varying magnitude M_t , given in Eq. (17), becomes

(A.2)

$$M_t = M_0 \left(1 - e^{-\frac{TR}{T_1}} \right) e^{-\frac{TE_t}{T_2^* + \delta z_t}} + x_t \beta_1$$

when the flip angle, ϕ , is assumed to be $\pi/2$ as in our calculations.

By substituting Eq. (A.2) into Eq. (A.1), the logarithm of the likelihood is

(A.3)

$$LL = -n \log(2\pi) - \sum_{t=1}^n \log r_t - n \log \sigma^2 - \frac{1}{2\sigma^2} \times \left[r_t^2 + (x'_{1t} \beta_1)^2 + \left(M_0 \left(1 - e^{-\frac{TR}{T_1}} \right) e^{-\frac{TE_t}{T_2^* + \delta z_t}} \right)^2 + 2(x'_{1t} \beta_1) \left(M_0 \left(1 - e^{-\frac{TR}{T_1}} \right) e^{-\frac{TE_t}{T_2^* + \delta z_t}} \right) - 2(x'_{1t} \beta_1) r_t \cos(\phi - \theta) - 2 \left(M_0 \left(1 - e^{-\frac{TR}{T_1}} \right) e^{-\frac{TE_t}{T_2^* + \delta z_t}} \right) r_t \cos(\phi - \theta) \right]$$

Eq. (A.3) can be alternatively represented by the vector multiplications as follows

(A.4)

$$LL = -n \log(2\pi) - \sum_{t=1}^n \log r_t - n \log \sigma^2 - \frac{1}{2\sigma^2} \left[\begin{array}{c} (r - X_1\beta_1)'(r - X_1\beta_1) + 2(r - r_*)'X_1\beta_1 \\ + (s_*M_0(1 - \exp(-TR/T_1)))' (s_*M_0(1 - \exp(-TR/T_1))) \\ + 2 (s_*M_0(1 - \exp(-TR/T_1)))' (X_1\beta_1 - r_*) \end{array} \right]$$

where r_* has t^{th} element of $r_t [\cos(\phi - \vartheta)]$, and s_* has t^{th} element of $\exp T \epsilon t T_2^* + \delta z t$.

Maximizing this likelihood with respect to the parameters is the same as maximizing the logarithm of the likelihood denoted LL with respect to the parameters and yields

(A.5)

$$\frac{\partial LL}{\partial M_0} = -\frac{1}{2\sigma^2} \left[2(1 - \exp(-TR/T_1))^2 M_0 s_*' s_* + 2(1 - \exp(-TR/T_1)) s_*' (X_1\beta_1 - r_*) \right]$$

(A.6)

$$\frac{\partial LL}{\partial T_1} = -\frac{1}{2\sigma^2} \left[2M_0^2 (-TR \exp(-TR/T_1)/T_1^2) (1 - \exp(-TR/T_1)) s_*' s_* + 2M_0 (-TR \exp(-TR/T_1)/T_1^2) s_*' (X_1\beta_1 - r_*) \right]$$

(A.7)

$$\frac{\partial LL}{\partial T_2^*} = -\frac{1}{\sigma^2} \left[M_0^2 (1 - \exp(-TR/T_1))^2 \left(\frac{\partial s_*}{\partial T_2^*} \right)' s_* + M_0 (1 - \exp(-TR/T_1)) \left(\frac{\partial s_*}{\partial T_2^*} \right)' (X_1\beta_1 - r_*) \right]$$

(A.8)

$$\frac{\partial LL}{\partial \delta} = -\frac{1}{\sigma^2} \left[M_0^2 (1 - \exp(-TR/T_1))^2 \left(\frac{\partial s_*}{\partial \delta} \right)' s_* + M_0 (1 - \exp(-TR/T_1)) \left(\frac{\partial s_*}{\partial \delta} \right)' (X_1\beta_1 - r_*) \right]$$

(A.9)

$$\frac{\partial LL}{\partial \beta_1} = -\frac{1}{2\sigma^2} \left[2X_1' r + 2X_1' X_1\beta_1 + 2X_1' (r - r_*) + 2M_0 (1 - \exp(-TR/T_1)) X_1' s_* \right]$$

(A.10)

$$\frac{\partial LL}{\partial \theta} = -\frac{1}{\sigma^2} \left[-(y_I \cos \theta - y_R \sin \theta)' (X_1\beta_1) - M_0 (1 - \exp(-TR/T_1)) (y_I \cos \theta - y_R \sin \theta)' s_* \right]$$

(A.11)

$$\frac{\partial LL}{\partial \sigma^2} = -\frac{n}{2} + \frac{1}{2(\sigma^2)^2} \left[\begin{array}{c} (r - X_1\beta_1)'(r - X_1\beta_1) + 2(r - r_*)'X_1\beta_1 \\ + (s_*M_0(1 - \exp(-TR/T_1)))' (s_*M_0(1 - \exp(-TR/T_1))) \\ + 2 (s_*M_0(1 - \exp(-TR/T_1)))' (X_1\beta_1 - r_*) \end{array} \right]$$

The CRLB for the variance of an unbiased estimate of a model parameter requires the symmetric Hessian matrix, generally denoted by H and is formed from second derivatives of the log likelihoods LL with respect to the model parameters. The second derivatives can be computed from the first derivatives of LL given in Eqs. (A.5), (A.6), (A.7), (A.8), (A.9), (A.10), (A.11).

The matrix of CRLBs can be found via the inverse of the Fisher information matrix. By taking expectations of the block elements of the Hessian matrices, the CRLBs can be found. The Fisher information matrices, generically

denoted by l , are $-E[H|M_0, T_1, T_2^*, \delta, \beta_1, \sigma^2]$ for the DeTeCT and DeTeCT-ING Models that are the expectation of the Hessian matrix H with respect to y_R and y_I given $M_0, T_1, T_2^*, \delta, \beta_1, \sigma^2$.

Appendix B. MLEs of the DeTeCT-ING Model under the Null Hypothesis

The MLEs of the DeTeCT-ING Model under the restricted null hypothesis, $H_0: T_1 = T_{1GM}, T_2 = T_{2GM}, \delta = 0$, are computed maximizing the likelihood with respect to parameters, M_0, β_1, ϑ and σ^2 . Maximizing this likelihood with respect to the parameters is the same as maximizing the logarithm of the likelihood, LL , with respect to the parameters. By setting the derivatives that are given in Eqs. (5), (9), (10), (11), equal to zero and solving, the MLE's under the null hypothesis can be found as follows

(B.1)

$$\hat{M}_0 = - \frac{(\hat{s}_*'(X_1\beta_1 - \hat{r}_*))}{(1 - \exp(-TR/T_{1GM}))(\hat{s}_*' \hat{s}_*)}$$

(B.2)

$$\hat{\beta}_1 = (X_1'X - X_1' \hat{s}_*(\hat{s}_*' \hat{s}_*)^{-1} \hat{s}_*' X_1')^{-1} (X_1' \hat{r}_* - X_1' \hat{s}_*(\hat{s}_*' \hat{s}_*)^{-1} \hat{s}_*' \hat{r}_*)$$

(B.3)

$$\frac{\partial \hat{r}_*}{\partial \hat{\theta}} \left[\hat{s}_* \hat{M}_0 (1 - \exp(-TR/T_{1GM})) + X_1 \hat{\beta}_1 \right] = 0$$

(B.4)

$$\hat{\sigma}^2 = \frac{1}{2n} \left[\begin{array}{c} (r - X_1 \hat{\beta}_1)'(r - X_1 \hat{\beta}_1) + 2(r - \hat{r}_*)' X_1 \hat{\beta}_1 \\ + \left(\hat{s}_* \hat{M}_0 (1 - \exp(-TR/T_{1GM})) \right)' \left(\hat{s}_* \hat{M}_0 (1 - \exp(-TR/T_{1GM})) \right) \\ + 2 \left(\hat{s}_* \hat{M}_0 (1 - \exp(-TR/T_{1GM})) \right)' (X_1 \hat{\beta}_1 - \hat{r}_*) \end{array} \right]$$

where \hat{r}_* has t^{th} element of $r_t[\cos(\phi - \vartheta)]$, and \hat{s}_* has t^{th} element of $\exp(T\epsilon T_2^* GM)$.

References

- [1] E.M. Haacke, R. Brown, M. Thompson, R. Venkatesan. Magnetic resonance imaging: physical principles and sequence design, John Wiley and Sons, New York (NY) (1999)
- [2] J.R. Roebuck, S.J. Haker, D. Mitsouras, F.J. Rybicki, C.M. Tempny, R.V. Mulkern. **Carr–Purcell–Meiboom–Gill imaging of prostate cancer: quantitative T_2 values for cancer discrimination.** Magn Reson Imaging, 27 (4) (2009), pp. 497-502
- [3] J.M. Bonny, M. Zanca, J.Y. Boire, A. Veyre. **T_2 maximum likelihood estimation from multiple spin-echo magnitude images.** Magn Reson Imaging, 36 (2) (1996), pp. 287-293
- [4] J.P. Haldar, J. Anderson, S.W. Sun. **Maximum likelihood estimation of T_1 relaxation parameters using VARPRO.** Proc Intl Soc Mag Reson Med, 15 (2007), p. 41
- [5] J. Liu, A. Nieminen, J.L. Koenig. **Calculation of T_1, T_2 and proton spin density in nuclear magnetic resonance imaging.** J Magn Reson, 85 (1) (1989), pp. 95-110
- [6] Y. Mazaheri, B.B. Biswal, B.D. Ward, J. Hyde. **Measurements of tissue T_1 spin-lattice relaxation time and discrimination of large draining veins using transient EPI data sets in BOLD-weighted fMRI acquisitions.** Neuroimage, 32 (2) (2006), pp. 603-615
- [7] J. Sijbers, A.J. den Dekker, E. Raman, D. Van Dyck. **Optimal estimation of T_2 maps from magnitude MR images.** Proc SPIE Med Imaging, 3338 (1998), pp. 384-390

- [8] J. Sijbers, A.J. den Dekker, E. Raman, D. Van Dyck. **Parameter estimation from magnitude MR images.** *Int J Imaging Syst Technol*, 10 (2) (1999), pp. 109-114
- [9] F. Baselice, G. Ferraioli, V. Pascazio. **Relaxation time estimation from complex magnetic resonance imaging.** *Sensors*, 10 (4) (2012), pp. 3611-3625
- [10] A.J. Wheaton, A. Borthakur, R. Reddy. **Application of the keyhole technique to $T_{1\rho}$ relaxation mapping.** *J Magn Reson Imaging*, 18 (6) (2003), pp. 745-749
- [11] S. Lai, G.H. Glover. **Detection of BOLD fMRI signals using complex data.** *Proc Intl Soc Mag Reson Med*, 5 (1997), p. 1671
- [12] F.Y. Nan, R.D. Nowak. **Generalized likelihood ratio detection for fMRI using complex data.** *IEEE Trans Med Imaging*, 18 (4) (1999), pp. 320-329
- [13] J.R. Reichenbach. **The future of susceptibility contrast for assessment of anatomy and function.** *Neuroimage*, 62 (2) (2012), pp. 1311-1315
- [14] D.B. Rowe, B.R. Logan. **A complex way to compute fMRI.** *Neuroimage*, 23 (3) (2004), pp. 1078-1092
- [15] D.B. Rowe, B.R. Logan. **Complex fMRI analysis with unrestricted phase is equivalent to a magnitude-only model.** *Neuroimage*, 24 (2) (2005), pp. 603-606
- [16] P. Bandettini, A. Jesmanowicz, E. Wong, J.S. Hyde. **Processing strategies for time-course data sets in functional MRI of the human brain.** *Magn Reson Med*, 30 (2) (1993), pp. 161-173
- [17] R.W. Cox, A. Jesmanowicz, J.S. Hyde. **Real-time functional magnetic resonance imaging.** *Magn Reson Med*, 33 (2) (1995), pp. 230-236
- [18] M.M. Karaman, I.P. Bruce, D.B. Rowe. **Incorporating simultaneously estimated T_1 and T_2^* of gray matter improves brain activation statistics in fMRI.** *Proc Int Soc Magn Reson Med* (2013), pp. 20-2285
- [19] T.A. Severini. *Likelihood methods in statistics*, Oxford University Press, Oxford (2001)
- [20] D.B. Rowe. **Modeling both the magnitude and phase of complex-valued fMRI data.** *Neuroimage*, 25 (2005), pp. 1310-1324
- [21] H. Gudbjartsson, S. Patz. **The Rician distribution of noisy data.** *Magn Reson Med*, 34 (6) (2005), pp. 910-914
- [22] S.O. Rice. **Mathematical analysis of random noise.** *Bell Systm Tech J*, 23 (1944), p. 282
- [23] Gach HM, Tanase C, Boada F. 2D & 3D Shepp–Logan phantom standards for MRI. ICSENG '08;521-526.
- [24] S.W. Atlas. *Magnetic resonance imaging of the brain and spine*, Williams & Wilkins, Lippincott (PA) (2008)
- [25] B.R. Logan, D.B. Rowe. **An evaluation of thresholding techniques in fMRI analysis.** *Neuroimage*, 22 (1) (2004), pp. 95-108
- [26] D.B. Rowe. **Parameter estimation in the magnitude-only and complex-valued fMRI data models.** *Neuroimage*, 25 (4) (2005), pp. 1124-1132
- [27] D.B. Rowe. **Magnitude and phase signal detection in complex-valued fMRI data.** *MagnReson Med*, 62 (5) (2009), pp. 1356-1357